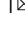## ARTICLE

Check for updates

Algorithm for fast evaluation of in-plane fiber orientation in reinforced plastics using light microscopy images

Klara Wiegel [1✉], André Schlink [2✉], Elisabeth Eckel [1], Mohamed Ayeb[1], Ludwig Brabetz[1], Michael Hartung[2] & Hans-Peter Heim[2]

Methods for evaluating the orientation of carbon fibers in reinforced plastics vary in complexity and are application specific. Here, we report an algorithm that quickly evaluates in-plane fiber orientation based on determining the correlation coefficient of adjacent regions in microscopy images. The result is not the fiber orientation of individual fibers, but the principal fiber orientation of small image areas. This method is applicable to large areas due to its low computation time and captures varying fiber orientations, making it suitable for the study of injection molded samples with complex geometries. A great advantage is that no information about the fibers or the matrix, or their combination, is needed prior to the analysis. This approach is also suitable for samples with surface defects. Demonstrations of this technique are given for Polyamide 6 and Polypropylene with 30 weight % carbon fibers of different fiber lengths.

[1] Electrical and Electronic Automotive Systems, University of Kassel, Wilhelmshöher Allee 73, 34121 Kassel, Germany. [2] Institute of Material Engineering, Polymer Engineering, University of Kassel, Mönchebergstraße 3, 34125 Kassel, Germany. ✉email: wiegel@uni-kassel.de; andre.schlink@uni-kassel.de

Carbon fiber reinforced plastics (CFRP) are already used in various sectors such as aerospace in the field of antistatic and are therefore often the subject of current research[1,2]. They have not yet been used for specific current conduction and still have a promising field of application in this area in the future. While the mechanical and chemical properties are well studied[3], research into the electrical properties is still in its infancy. In order to investigate electrical properties or to describe them mathematically, knowledge of the fiber orientation is essential, since the current flow is mainly confined to the fibers and thus directly depending on the fiber orientation. The importance of the fiber orientation regarding the electrical resistance and contact properties of injection-molded CFRP has been demonstrated in several scientific papers[4–6]. The electrical conductivity of CFRP requires that the carbon fibers form a network (percolation network)[7,8], since only fibers that are in physical contact or close to each other (tunneling effect) are able to conduct current. In addition to a filler content above the percolation threshold, network formation can be locally enhanced by appropriate fiber orientation.

There are a number of methods for determining the fiber orientation of fiber-reinforced plastics (such as carbon or glass fiber polymer compounds) and good summarizations can be found in[9–12]. These methods are optimized for their specific application and they vary in complexity.

The method of choice to obtain a 3D orientation is usually based on micro-computed tomography, e.g. combined with the determination of the elliptical parameters of the fiber cross section[13–16] and the use of tracing techniques such as digital image correlation[12]. Micro-computed tomography is a time-consuming method and the area observed is typically small, in the μm range. A faster approach has been proposed in[17], where ultrasound scans are used to obtain the necessary, in this case, 2D image information (with a scanning velocity of 20 mm/s), but with a spatial resolution of 0.25 mm, providing only general information on fiber orientation. The same applies to the eddy current method[18,19], where fiber orientations of large areas of several mm were analysed, but again with an increment size of 0.2 mm − 0.25 mm. The resolution of the principal fiber orientation calculated with the algorithm presented here depends on the resolution of the input image (here microscopic images of several cm) and the available computational time, typical resulting increments were found to be around 0.04 mm. The focus of this work is on microscopic images, but the algorithm is not restricted to these, any 2D images of fibers could be used. The level of detail in the output of the presented algorithm can be placed between the highly detailed but small area limited micro computed tomography scans and the coarser resolution of large areas as in the case of eddy current or ultrasound scans.

Nonetheless, the above methods as the method presented here (light microscopy) need post processing to retain the fiber orientation. Common image processing techniques are Radon transforms[20–22], Gabor filters[17,23] or 2D Fast Fourier Transform[19,24,25]. Comparing the number of mathematical operations required, all of the above methods are more complex than the algorithm presented here and hence are more time consuming in comparison. In most cases the application of said methods is the deviation of uniform fiber orientations, the algorithm presented in this work explicitly addresses the case of non-uniform fiber orientation of areas several square centimeters in size.

When the knowledge of the 2D orientation is sufficient, the most common application is to check for misalignment for quality control or feature prediction, which simplifies the complexity of the problem, because the nominal orientation is known. For example, Creighton et al.[26] developed a method to derive the orientation from elongated features in an image. The black-and-white microscopy images contained parallel, in-plane fibers. At defined pixel positions, a virtual fiber resembling a pixel array with a given length was rotated by different degrees along its center and the intensity in this area was summarized. The intensity minimum of all angles indicates the orientation of the fiber at that position. Sutcliffe et al.[27] improved this method in terms of speed and functionality, including combining it with an autocorrelation function to determine the dimensions of the misaligned regions.

In addition to the experimental quantification of the fiber orientation, it is also possible to simulate an injection molding process including the resulting fiber orientations. Simulated results do not provide an exact image of the real conditions, since the underlying material model and its input variables are decisive here. The disadvantages here are the need for information on fiber parameters and the rheological properties of the plastic melt[28].

The method presented here is in some ways similar to the work of Creighton and Sutcliffe but does not require the knowledge of fiber dimensions. Instead of comparing the concordance of a virtual fiber with an image detail, only image areas are compared. The theory is that adjacent image areas shifted along the fiber direction will have a higher correlation than image areas shifted out of the fiber direction. The advantage of this method is its speed and therefore its applicability to large areas of several square centimeters. The calculation time always depends on the calculation parameters and of course on the desired accuracy. An average calculation time of 30 s/mm² was achieved with still very good detail information. In addition, no fiber parameters need to be known in advance and it is not necessary for all fibers to lie largely in the plane of observation, making it applicable to any injection-molded specimen with highly variable fiber orientations. It should be noted that fiber orientations outside the observed plane are not detected by this method. The result is not the fiber orientation of individual fibers, but the principal fiber orientation at a given pixel position. This work is part of a preliminary effort to describe the electrical resistance network of injection-molded parts.

Results

Sample preparation for high-resolution microscopic imaging. To create suitable test specimens for the analysis by means of the algorithm presented here, they were manufactured by insert injection molding. Fig. 1a indicates the melt flow of the manufacturing process. The specimens consist of carbon fiber reinforced composites with polypropylene and polyamide 6 matrix (PP CF30 and PA CF30). A specific fiber orientation is generated within the specimens by the special mold geometry, such as around the inserts as shown in Fig. 1b and d. After the manufacturing process, the specimens were prepared in an epoxy resin, which is shown in Fig. 1c and high-resolution microscopic images were generated. The entire preparation process is precisely described in the Methods section.

Algorithm. The method is implemented in Matlab (Matlab R2022b, Mathworks, Natick, MA, USA). The developed algorithm rasterizes image areas and assigns a principal fiber orientation to each area. Masked areas are ignored. The central pixel of the area determines the position to which the orientation is assigned. This means that the fiber orientation can even be determined on a pixel-by-pixel basis, but in most cases, this is not necessary since fiber orientations tend to change continuously.

To determine the fiber orientation, the algorithm starts with an area of interest (AOI) of a predefined size containing $n \times n$ px. It
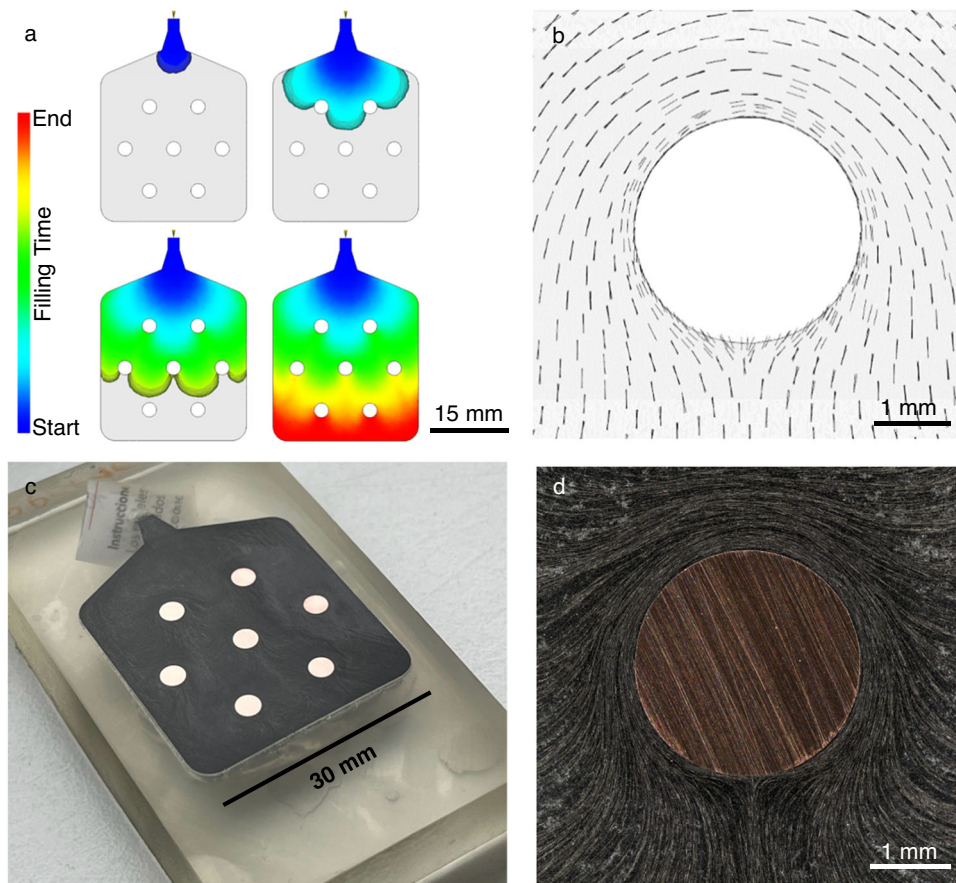
Fig. 1 Flow situation and preparation of the specimens. a Result of the flow analysis at four points in time. **b** Resulting fiber orientation around the central insert, indicated by lines. **c** Prepared embedded specimen. **d** Microscopic image section of the central insert of the PP CF30 specimen, showing the expected varying fiber orientations.

then determines adjacent regions A_θ (with the same size) that are shifted by a defined offset d in different angular steps $\Delta\theta$, which represent possible fiber orientations. An overview of these parameters is shown in Fig. 2 with an example image area of 2 × 2 mm. Specimen used here was PP CF30.

If the derived fiber orientations need to be particularly accurate, a small $\Delta\theta$ should be used. It is also necessary for d to have a minimum value to represent each angle position properly. For calculating displacement, pixels are considered square. Therefore, in order to calculate distances in pixel equivalents at defined angles, defined pixel combinations in x and y must be possible. Fig. 2e, f illustrate this discretization problem.

When all adjacent regions A_θ are defined, the Pearson correlation coefficient R_θ between AOI and every A_θ is calculated using:

$$R_\theta = \frac{\sum_i \left(\text{AOI}_i - \overline{\text{AOI}}\right)\left(A_{\theta i} - \overline{A_\theta}\right)}{\sqrt{\sum_i \left(\text{AOI}_i - \overline{\text{AOI}}\right)^2 \sum_i \left(A_{\theta i} - \overline{A_\theta}\right)^2}} \quad (1)$$

where AOI_i is the grayscale value of each pixel element of the AOI with $\overline{\text{AOI}}$ being its mean value, and $A_{\theta i}$ is the grayscale value of each pixel element of the A_θ under consideration whose mean value is $\overline{A_\theta}$. By definition, a high correlation would be achieved when the grayscale values in both areas are similar for the same pixel elements (i.e., have comparable fibers in length, diameter, and orientation at that location). For example, if a pixel of the AOI, i.e., the center pixel, is placed directly on a fiber, and the same pixel element of the A_θ is also placed along the same fiber, this would result in at least some of the surrounding elements

having the same grayscale values (the values along that fiber). The remaining elements do not necessarily have to match, since the fibers are statistically scattered and direct overlap is unlikely, but of course, it would also increase the correlation.

In accordance with the angular equivalence (see Fig. 2b), two maxima are expected, separated by 180°. The result for the example shown in Fig. 3a is very promising and shows, as expected, two maxima separated by 180°. The resulting principal fiber orientation for this area is shown in Fig. 3b.

For continuity, all following values ≥180° are assigned to their equivalents in the range 0–179°. If the fibers are densely packed, it is also possible, to have a high degree of correlation perpendicular to the fiber direction. This effect can be compensated by choosing a larger n.

The next step is to select the next AOI based on the next center pixel. This can be an immediately adjacent pixel or a slightly offset one, depending on the desired resolution. Fig. 3c, d is showing the result for the whole area shown in Fig. 2c. In the absence of another validation method, the validation was done only visually. The concordance with the microscopic image is very good, even in the areas of the curved edges.

This calculation was performed on an Intel Xeon E5-1650 v3 2 × 350 GHz processor using the parallel computing toolbox of Matlab. For ten runs, the mean computation time was 36.2 s (mean CPU time was 0.68 s) for a 2 × 2 mm image (1001 × 1001 px). The masked area covers 42 % of the image, resulting in an effective area of 2.3 mm². To avoid computational overhead in Matlab, the memory access for this algorithm was optimized using global variables.
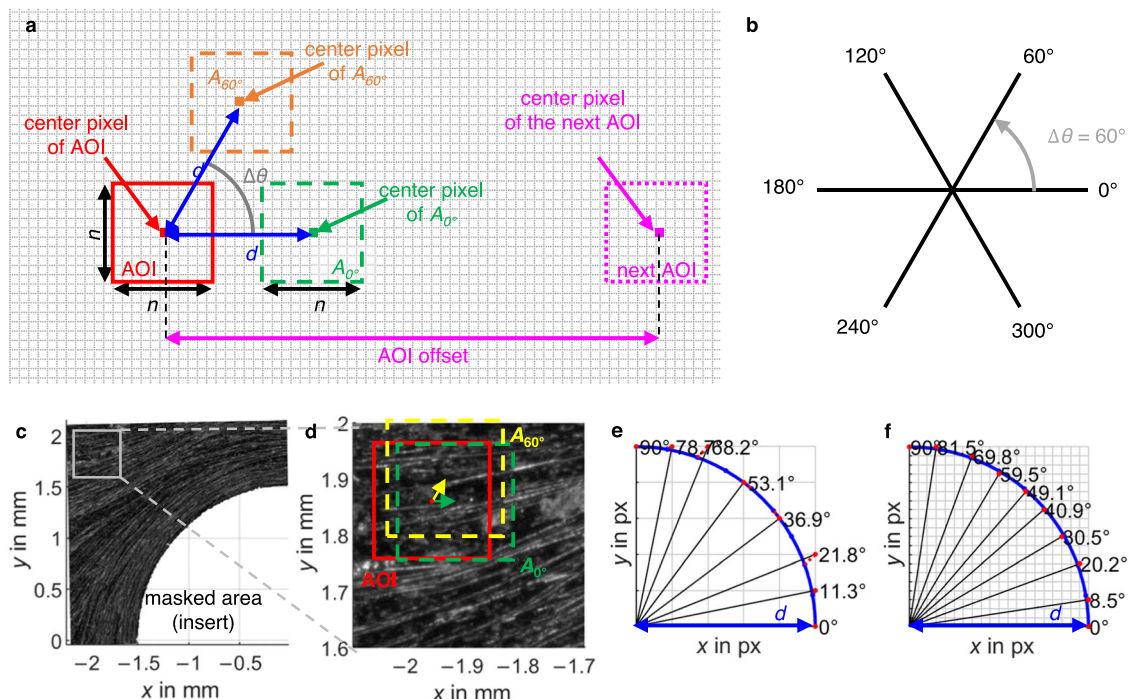
Fig. 2 Algorithm parameters. a Exemplary overview: the AOI, defined by its center pixel position and the edge length n; the displacement d between the AOI and its neighboring A_θ (dashed boxes); the angle increment $\Delta\theta$, which defines together with d the positions of the neighboring A_θ, here $A_{0°}$ and $A_{60°}$; and the AOI offset, which defines the position of the next AOI, here shown only in horizontal direction. The grid background represents square pixels. In **b** the angle definitions are shown. Angles are specified counterclockwise. There is an equivalence between the angles. A fiber orientation of 0° is equivalent to 180°, 60° to 240° etc. The example $\Delta\theta$ is marked in gray with its resulting values for θ. **c** The same definitions illustrated using an example image (reprinted with Matlab in grayscale) of a PP CF30 specimen containing fibers with different fiber orientations. An enlarged section shows **d**, where the AOI is an area of 101 × 101 px (0.21 × 0.21 mm), marked by a red box with a red dot as the center pixel. Two exemplarily adjacent regions are shown in green ($A_{0°}$) and yellow ($A_{60°}$), where the index represents the displacement angle θ in the angular direction and is marked with an arrow of the corresponding color with $d = 20$ px. Under the conditions that **e** $d = 5$ px, $\theta = 10°$ and **f** $d = 20$ px, $\theta = 10°$, the feasible angles θ (in the range from 0–90°) are shown. The grid represents discrete pixels. The blue arc represents a quarter circle with the radius = displacement d. To satisfy the condition of $\Delta\theta = 10°$, all neighboring center pixels should be on this arc. These positions are marked by blue diamonds. Since pixels are discrete objects, the nearest pixel positions are chosen instead. The position offset is marked with red dotted lines. It is obvious, that the angle increment of 10° in the case of $d = 5$ px is poorly fulfilled. A larger d allows for a more evenly distribution of θ, as shown in **f**.

Parameter evaluation. Parameter sweeps were performed to determine the influence of the calculation parameters for the same image area as before. The sweep result for varying n (which determines the size of the AOI) is shown in Fig. 4. Decreasing n leads to increasing artifacts in the fiber orientation determination. To avoid this, n should be greater than the size of any groups of interfering objects such as voids, air entrapments and other defects. On the other hand, increasing n results in a loss of detail because the AOI covers a larger area, resulting in a coarser principal fiber orientation. Since size specifications for the parameters in pixels depend on the image resolution, they are specified in mm from here on. Suggested values for n should be >0.2 mm. Note that as n increases, so does the computation time. In general, the algorithm runs in O(N) time, where N is the number of pixel elements in the AOI. Since the AOI is quadratic in this case, N is defined by n, $N = n^2$.

The results of varying the displacement d for A_θ are shown in Fig. 5a. As mentioned above, a too small d leads to a coarser distribution of feasible angles θ and thus to a loss of information. Conversely, if d is chosen too large, this will lead to the formation of artifacts because the correlated AOI and its A_θ will be further apart and the calculated fiber orientation will be falsified. The suggestion for d is about 0.04 mm. Changing d does not affect the calculation time.

Varying $\Delta\theta$ predefines the number of fiber orientations that can be determined. Varying the offset between the AOI only

affects the resulting resolution. Both parameters should be adjusted according to the application.

To evaluate the required minimum image resolution, the resolution of the example image was gradually reduced by bicubic interpolation using the Matlab function 'imresize'. The results are shown in Fig. 5b. Reducing the resolution results in a gradual loss of information because the computational parameters decrease at the same time, as they are resolution dependent. However, the main features of the principal fiber orientation are still resolved with an image with 20 % of the original size (97 px per mm). A good level of information is obtained at 60 % (292 px per mm). If a $\Delta\theta$ of 10° is sufficient, the image resolution and thus computation time can be significantly reduced.

The selected sample geometry allows for a variety of fiber orientations to be examined. The total examination areas are about 30 × 30 mm each, which is quite large, so the results will initially focus on the more challenging parts of the image. Starting with specimen PP CF30. An overview of the focus areas i-iv is shown in Fig. 6a.

The calculated principal fiber orientation for area i is shown in Fig. 6b. Area i contains an agglomeration of fibers causing an abrupt orientation change that the algorithm handles well. For this calculation, n must be increased because there are many grouped interfering voids. Area ii (s. Fig. 7a) contains an area with only few fibers. Where there are adjacent fibers with a uniform orientation, the algorithm performs well. Where there are only few in-plane
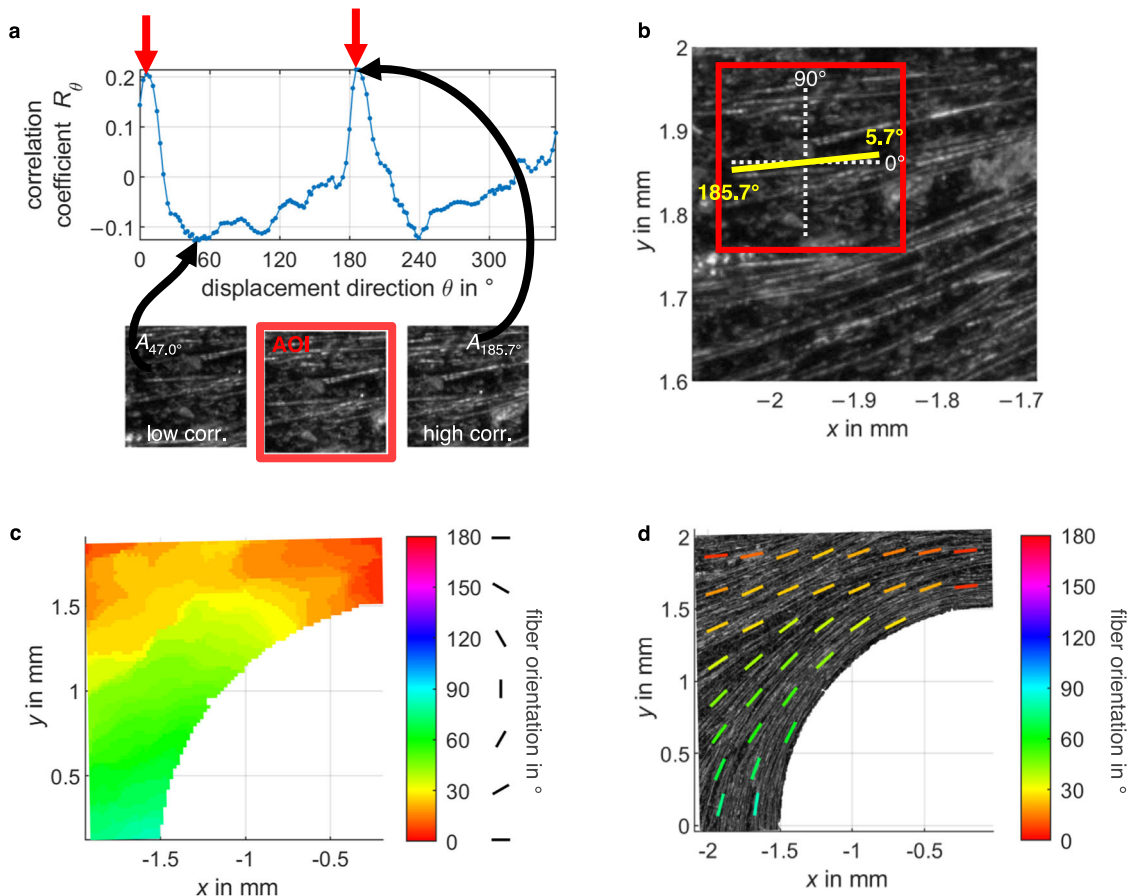
Fig. 3 Correlation coefficient and resulting fiber orientation. a shows the calculated correlation coefficient R_θ for all displacement directions. The angular increment $\Delta\theta$ was chosen to be 1° in this example. According to the angular equivalence, there are two local maxima at 5.7 and 185.7° (marked with red arrows). In addition, three areas are shown, the example AOI and two A_θ (one with a low and one with a high R_θ value). **b** The main fiber orientation determined for this example AOI (red) is shown in yellow. **c** The principal fiber orientations of the sample image shown using the presented image correlation algorithm, represented by areas and **d** by virtual fibers that are displaying the same data on a uniform grid. The microscopy image from the above example forms the background, reprinted in grayscale. The virtual fibers represent the principal fiber orientation of the surrounding area. This representation is intended to provide an easier way to evaluate the result of the principal fiber orientation visually. The calculation parameters chosen were $n = 101$ px (0.21 mm), $d = 20$ px (0.041 mm), $\Delta\theta = 1°$ and the AOI offset $= 10$ px (0.021 mm).
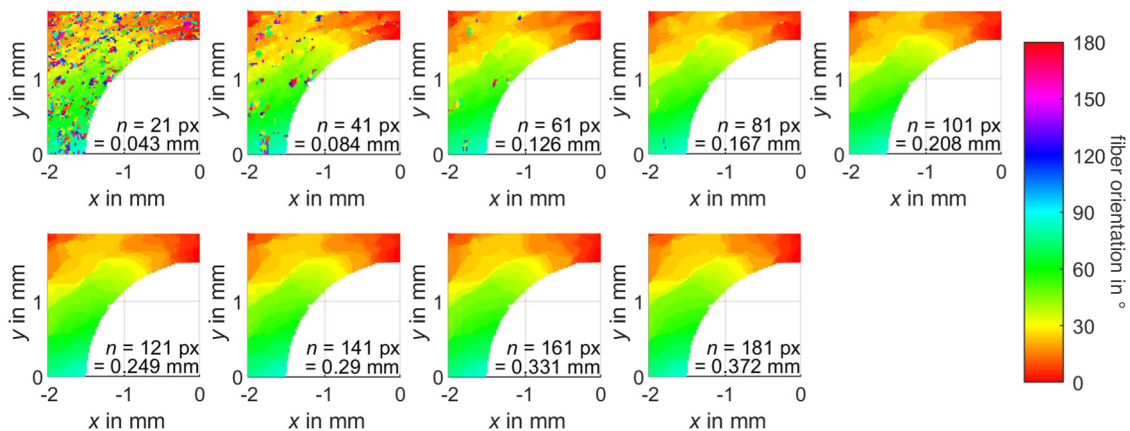

Fig. 4 Principal fiber orientation calculated with varying size $n \times n$ of AOI. A decreasing n leads to artifacts in the fiber orientation determination. An increasing n leads to a loss of detail. The remaining parameters of the calculation $d = 20$ px (0.041 mm), $\Delta\theta = 1°$ and the AOI offset $= 10$ px (0.021 mm).

fibers with a random orientation (such as the incipient weld line), the algorithm will only calculate a coarse orientation as the AOI is too large to capture all the detail. If the orientation of these few fibers is important, n can be decreased and the orientation will be better represented, s. Fig. 7b. Note, the algorithm does not calculate

individual fiber orientations and does not specify whether fibers are present or not. The calculated principal fiber orientation for area iii is shown in Fig. 7c. The slow, continuous orientation change is well represented all around the insert, even in the area of the incipient weld line. Areas of a locally confined continuous orientation
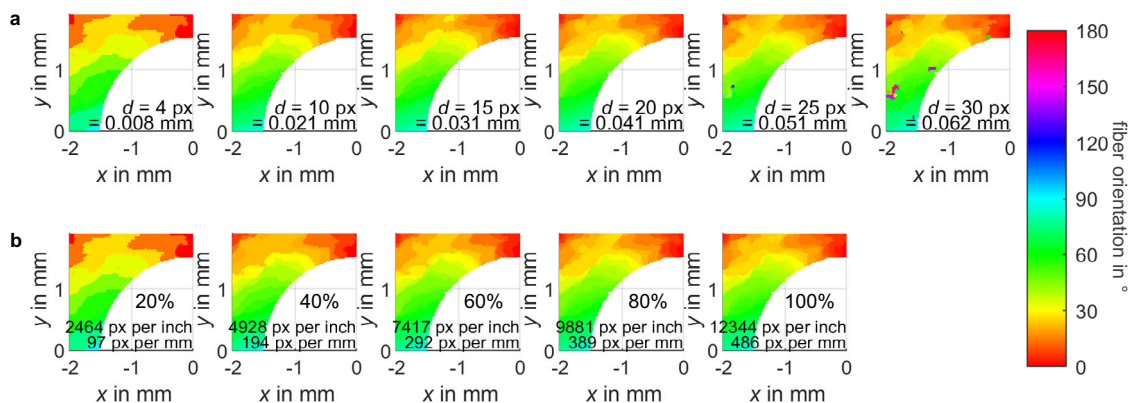
Fig. 5 Principal fiber orientation calculated with varying displacement d of A_θ and at reduced resolutions. a A decreasing d leads to a loss of information. An increasing d leads to artifact formation. The remaining parameters of the calculation were $n = 101$ px (0.21 mm), $\Delta\theta = 1°$ and the AOI offset = 10 px (0.021 mm). **b** The resolutions are indicated by the percentage in each image relative to the source image. Reducing the resolution results in a gradual loss of information. A good information detail is still obtained at 60 %. The calculation parameters were $n = 0.21$ mm, $d = 0.041$ mm, $\Delta\theta = 1°$ and the AOI offset = 0.021 mm.
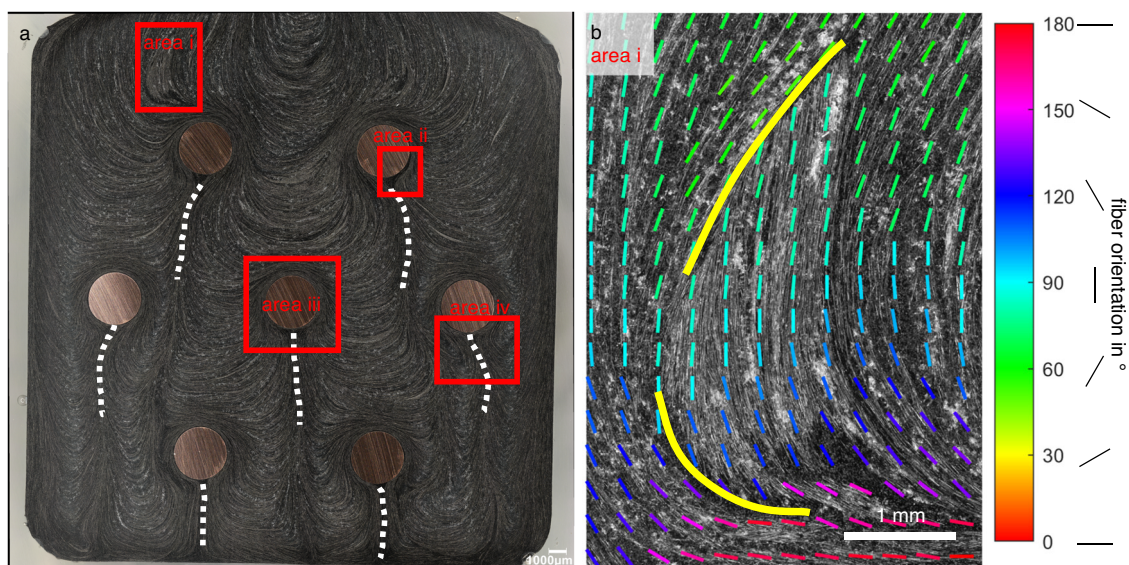

Fig. 6 Microscopic image with characteristic areas and corresponding principal fiber orientations. a Microscopic image of the PP CF30 specimen. Different fiber orientations are clearly visible, which are caused by the injection molding process. Weld lines are indicated by white dotted lines. In this material, there are many groups of interfering small surface defects due to voids in the polymer compound (light gray specks). The areas for more detailed evaluation are marked with red boxes. Area i contains an agglomeration of fibers with an abrupt change in orientation. Area ii contains an area with only few in-plane fibers. Area iii contains the orientations around an insert including the incipient weld line. Area iv contains gradually changing fiber orientations in a small area. **b** The principal fiber orientation for area i. The abrupt change in orientation is marked with two yellow lines. This change is well captured by the algorithm. The calculation parameters were $n = 0.29$ mm, $d = 0.041$ mm, $\Delta\theta = 1°$ and the AOI offset = 0.021 mm.

change, such as area iv (s. Fig. 7d), are again roughly represented with the given calculation parameters. Reducing n brings only a small improvement, as there are too many interfering surface defects in this example area.

The total principal fiber orientation for the whole specimen is shown in Fig. 8. The parameter n was slightly increased, since many interfering objects were present in the image, so locally restricted continuous orientation changes are interpreted as abrupt. Otherwise, all orientations are well represented, including weld lines and border regions.

The resulting principal fiber orientation of the second specimen, PA CF30, is shown in Fig. 9. As the specimen geometry is identical, the main features of the fiber orientation, such as weld line formation, are similar and well represented. The difference between the two specimens is the polymer matrix, polyamide 6 vs. polypropylene, and the average fiber length, 510 vs. 185 μm

(factor ~2.7), making this algorithm applicable to different polymer materials and fiber lengths. Another difference is the presence of many big air entrapments in this specimen, especially the large group near the central insert. Increasing the parameter n can also be used as a filter for this kind of disruptions.

Stress testing. A random specimen of a glass fiber composite with a flow obstacle was used to stress test the algorithm. The authors have no information on the fiber or polymer parameters contained in the specimen. The micrograph of the prepared specimen is shown in Fig. 10a. The obvious differences from the other specimen are a comparatively poorer contrast between fiber and polymer matrix due to the transparency of the glass fibers, varying fiber lengths due to in-process breaking, few long in-plane fibers, and varying background intensities. The calculated principal fiber orientation is shown in Fig. 10b. Although the
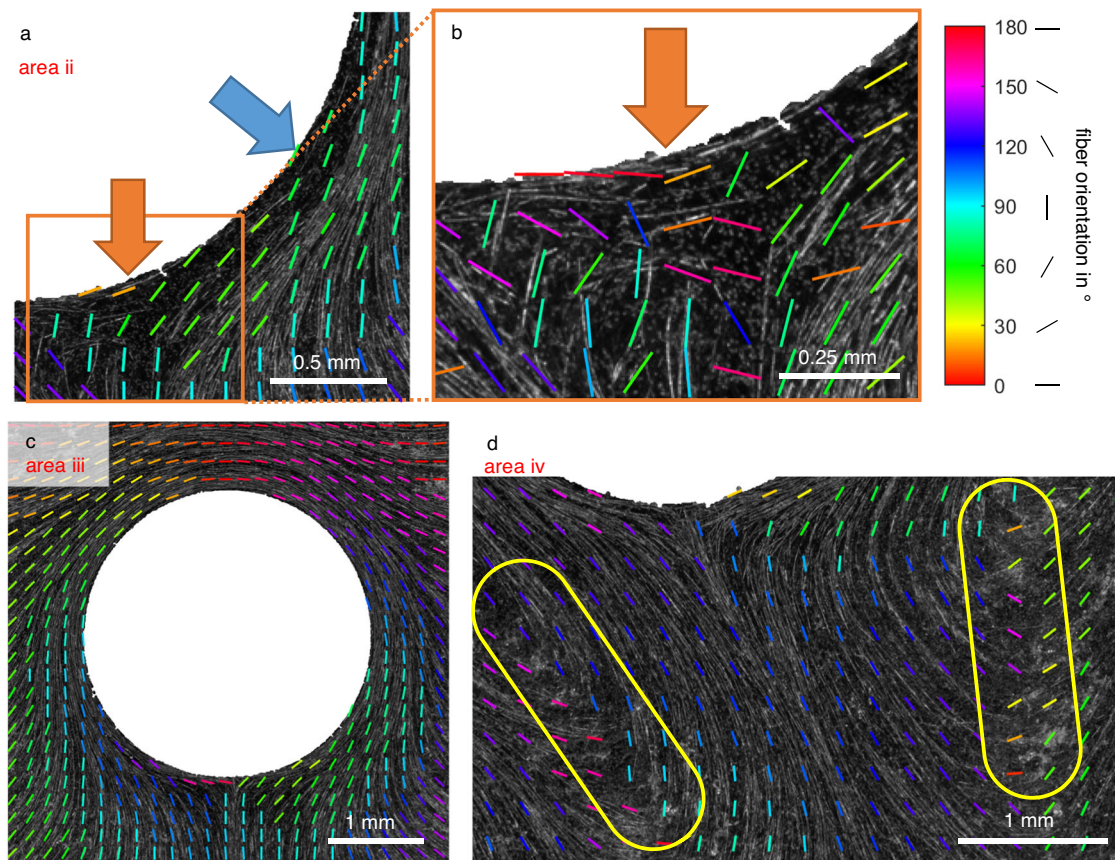
Fig. 7 Fiber orientation of challenging image areas. a The principal fiber orientation for area ii, using the same calculation parameters as for area i. Areas with few in-plane fibers with mostly uniform fiber orientation are well represented (blue arrow). Low-fiber areas with chaotic orientations are only roughly rendered (orange arrow). **b** Principal fiber orientation for area ii, showing only the area with a chaotic fiber orientation (orange box), using a reduced $n = 0.041$ mm for the calculation. Note that this evaluation shows virtual fibers on a regular grid, not actual fibers. **c** The principal fiber orientation for area iii. The calculation parameters were $n = 0.31$ mm, $d = 0.041$ mm, $\Delta\theta = 1°$ and the AOI offset $= 0.021$ mm. **d** The principal fiber orientation for area iv, using the same calculation parameters as for area iii. Areas with stronger continuous change in orientation are again only roughly rendered (marked in yellow).
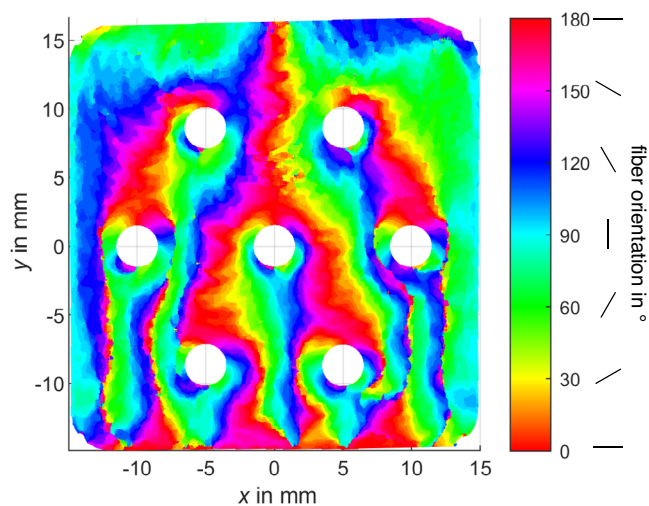

Fig. 8 Calculated principal fiber orientation of specimen PP CF30. The calculation parameters were $n = 0.25$ mm, $d = 0.041$ mm, $\Delta\theta = 1°$ and the AOI offset $= 0.041$ mm. The source image resolution was reduced to 292 px per mm.

image is challenging, the result is good. The fiber orientation around the flow obstacle with the weld-line is well captured as in the previous images, see Fig. 10c. Note that similar background intensities can lead to a higher correlation, but this effect seems to

be small. However, if adjacent fibers have distinct orientations, the fibers covering the larger area will dominate the resulting principal fiber orientation. There are many areas of such chaotic principal fiber orientation, but a closer inspection confirms this result, see Fig. 10d, e. Closely grouped similar objects will also have a high correlation coefficient along the group, leading to an erroneous result, see Fig. 10f. However, as mentioned above, this can be resolved by increasing n (from 0.24 mm to 0.42 mm), compare Fig. 10g. One limitation is areas without in-plane fibers. But again, this can be solved by increasing n. Increasing n would result in an increased AOI and therefore increase the probability of having in-plane fibers.

This specimen was chosen to test the algorithm and the result is remarkably fine. Note that this specimen has no interfering surface defects, which is an advantage. Due to the numerical approach, the poorer contrast is not a problem. Varying fiber lengths in the same image are also not a problem. A $n < 0.24$ mm is not recommended here, because of the low fiber density with many voids, which would result in a random orientation as the polymer material correlates in all directions. In this case the recommended value for n is 0.42 mm.

Discussion

The study presented here only covers a few different materials but shows that the algorithm is well applicable in all cases. It can also be applied without knowledge of the material properties as shown
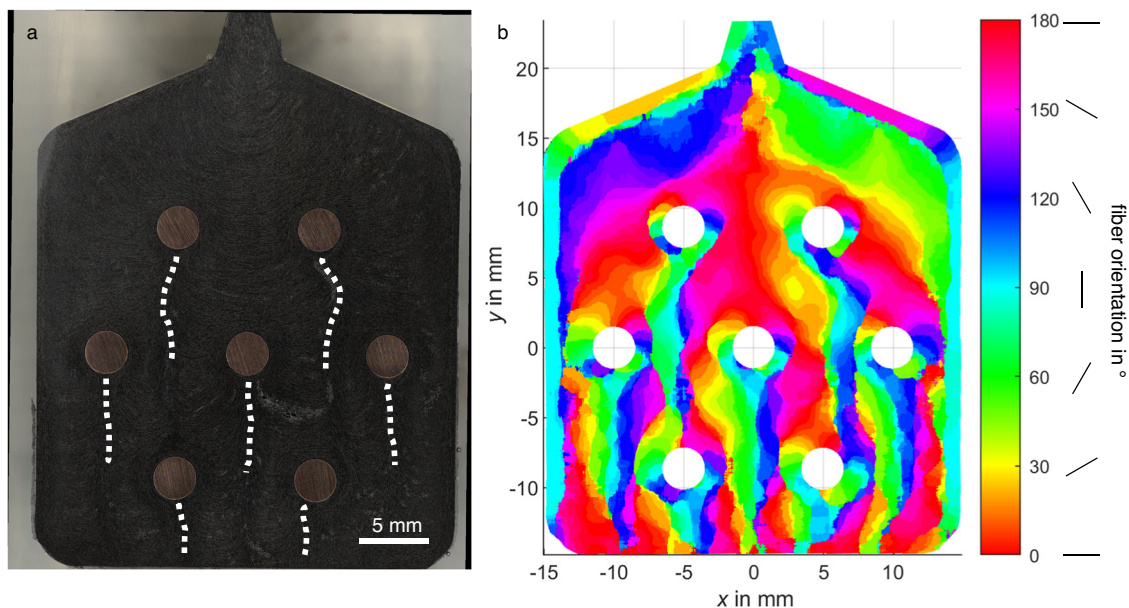
Fig. 9 Microscopic image and calculated principal fiber orientation of specimen PA CF30. a Weld lines are marked with white dotted lines. **b** The calculated principal fiber orientation of specimen PA CF30. The calculation parameters were $n = 0.62$ mm, $d = 0.041$ mm, $\Delta\theta = 3°$ and the AOI offset $= 0.041$ mm. The source image resolution was reduced to 292 px per mm. The parameter n was increased because of the presence of big air entrapments throughout the observation area due to the nature of the sample.

in the previous section. Due to the computation time, it can even be applied to large areas of several centimeters, as shown in this study. This allows an efficient quantitative visualization of the principal fiber orientation across the investigated plane with high resolution. Alternative quantitative methods, such as X-ray microcomputed tomography, have their limitations in terms of the size of the measurement area that can be covered and the time and effort required to evaluate the orientations. As an outlook, a comparative analysis of orientation tensors generated by injection molding simulation software based on these results is possible in order to obtain effective benchmarks for real fiber orientations.

The limits of use are small areas with strong changes in orientation. This is due to the size of the AOI. If it is larger than the area of the change, the fiber orientation cannot be properly represented and will be interpreted as abrupt. If it is small, interfering image details such as air entrapments, voids or other defects will distort the result. In general, interfering objects in an image pose a challenge to any type of algorithm.

Another limitation is areas with few fibers, especially if the fibers are short or only visible as elliptical cross sections; if these objects are grouped, misinterpretation of the principal fiber orientation is likely.

The algorithm presented here can be used with big AOI sizes to represent principal fiber orientations of large areas with slow continuous or abrupt changes. For a more detailed analysis, small AOI sizes are recommended. Thus, the same method can be used to quickly compute in-plane fiber orientations of large areas or perform detailed analysis to capture changes in small areas, such as chaotic orientations.

Conclusion

In summary, a fast method has been developed to evaluate fiber orientations from high resolution microscopic images of fiber filled materials. This method has a different approach from existing methods, which brings some advantages. Particularly noteworthy is the ability to evaluate the principal fiber orientations without prior knowledge of material parameters. This algorithm is not limited to microscopic images or injection

molded materials, any image containing fibers could be analyzed, since only correlations of image areas are considered. Furthermore, the computation time is very short, so that even large areas of several square centimeters can be calculated efficiently with high resolution (average computation time of 30 s/mm²). The level of information is lower than with micro-computed tomography based methods, but higher than with eddy current or ultrasound based methods. The latter is really effective with unidirectional layers. This algorithm is intended for the analysis of large areas of non-unidirectional injection molded materials.

Methods

Materials. Two semi-crystalline carbon fiber-filled polymer compounds were used for the preparation of the testing samples. The first one of those, is a self-compounded material (PP CF30) made of polypropylene (PP 520 P, SABIC, Riyadh, Saudi Arabia) compounded with 30 weight % carbon fiber (SIGRAFIL C C6-4.0/240-T130, SGL CARBON, Wiesbaden, Germany). Based on the data sheet, the cut carbon fibers have a diameter of 7 µm and a length of 6 mm. They are coated with a polyurethane sizing to ensure compatibility with polypropylene matrices. Compounding was carried out using a co-rotating twin-screw extruder (ZSE 18 HPe, Leistritz, Nuremberg, Germany) with a screw diameter of 18 mm and a length-to-diameter ratio of 40. The screw configuration consists exclusively of conveying elements after the feeding zone, so that the fiber length reduction is kept low. Gravimetric feeders were used to add both components to the extrusion process. Carbon fibers were added via a side feeder. The temperature profile of the extrusion process can be viewed in Table 1. A throughput of 4.5 kg/h was set at a screw speed of 210 rpm. The fiber length in the resulting compound, determined by dynamic image analysis (QICPIC/R06, Sympatec, Clausthal-Zellerfeld, Germany), is ~510 µm.

As a second material, a commercially available polyamide 6 with 30 weight % carbon fibers was selected (PA CF30; Durethan BCF30H2.0EF 900111, LANXESS, Cologne, Germany), which differs strongly in the average carbon fiber length, 185 µm, in comparison to PP CF30. The fiber diameter was determined by
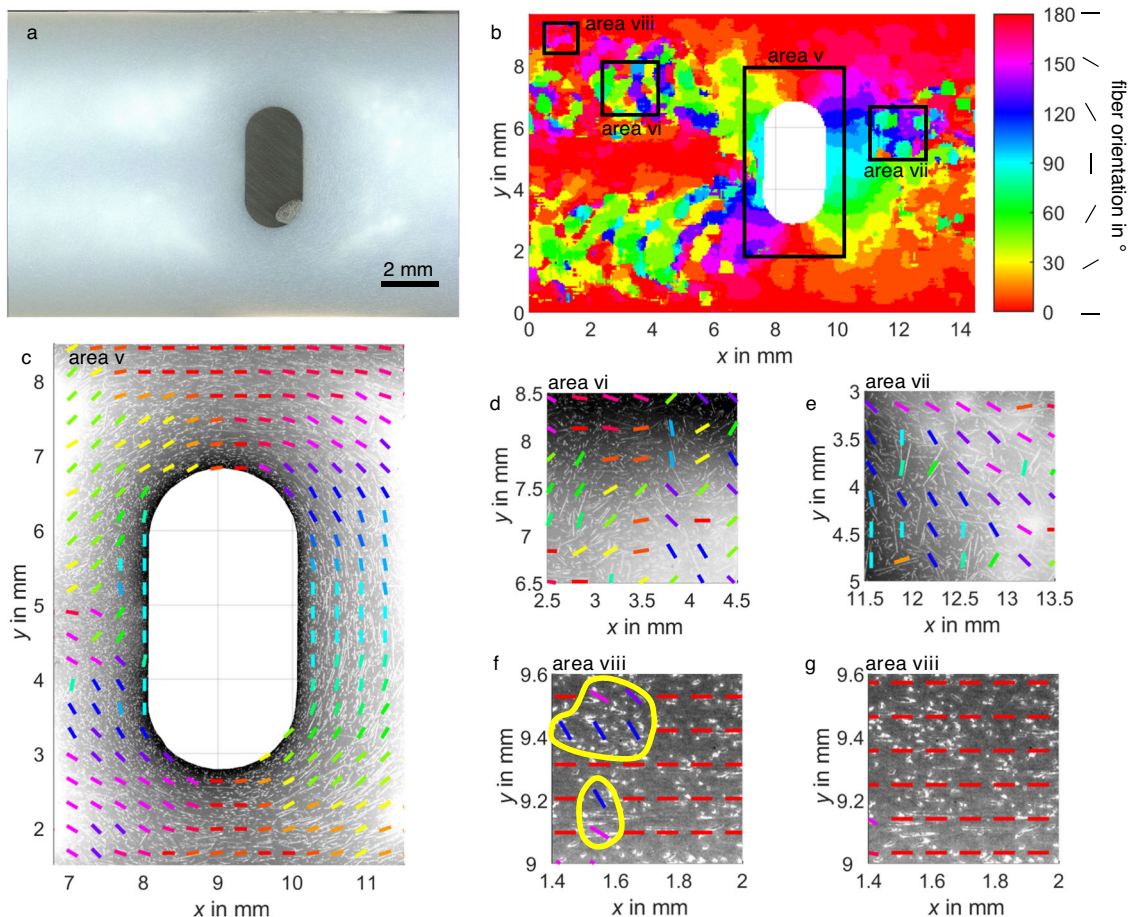
Fig. 10 Microscopic image and calculated principal fiber orientation of glass fiber composite specimen. a Microscopic image, the specimen size is 16 mm × 10.6 mm with a 2 mm × 4 mm flow obstacle. **b** The calculated areal principal fiber orientation of this specimen. The calculation parameters are $n = 0.24$ mm, $d = 0.02$ mm, $\Delta\theta = 5°$ and the AOI offset $= 0.054$ mm. The resolution of the source image was reduced to 295 px per mm. The areas for more detailed evaluation are marked with boxes. **c** The principal fiber orientation for area v (around the flow obstacle), and two exemplary chaotic areas, **d** area vi and **e** area vii. **f** Incorrect principal fiber orientations of area viii (encircled areas). Small in-line grouped fiber cross sections cause a high correlation along the group. **g** Result for the same area with an increased $n = 0.42$ mm. **c**–**g** are shown with adjusted contrast for a better fiber visibility in each area.

Table 1 Temperature settings of the extrusion process.

Extrusion zone	1	2	3	4	5	6	7	Nozzle	Melt temperature[a]
Temperature in °C	150	200	200	200	200	200	200	200	211

[a]Measured by a temperature sensor mounted inside the die.

scanning electron microscopy on a cryo-fractured sample and is ~7.5 μm.

In order to obtain a specific fiber orientation, which includes distinct areas for the fiber orientation evaluation, seven metal pins are inserted into a customized injection mold. These are intended to act as flow obstacles, around which the plastic melt is forced to flow. For this purpose, countersunk copper rivets according to DIN 661 with a diameter of 3 mm were used. The copper pins were tin-plated to ensure an identical surface. Before chemical tinning, the copper(II) oxide on the surface of the copper rivets is removed by immersion in 25 % acetic acid for 2 h. The tinning solution was prepared with tin powder (Seno 3211, BESTCHEM, Linsengericht, Germany). The tinning process was carried out according to the manufacturer's instructions. Subsequently the heads of the rivets were cut off with a diamond wire saw (Model 6234, WELL Diamond Wire

Saws, Mannheim, Germany), so that the resulting copper pins could be inserted into the cavity.

Injection molding. The samples were produced with a laboratory piston injection molding machine (HAAKE MiniJet II, Thermo Fisher Scientific, Waltham, MA, USA). A modular mold was developed for this purpose. It offers the possibility of integrating seven inserts, which are held in position by an elastomer spring element. One half of the mold and the dimensions of the corresponding specimen are shown in Fig. 11. The injection molding parameters are listed in Table 2.

Specimen preparation. After production, the individual specimens were embedded in a two-component casting resin system (Araldite DBF & Aradur HY 956 EN hardener, Huntsman
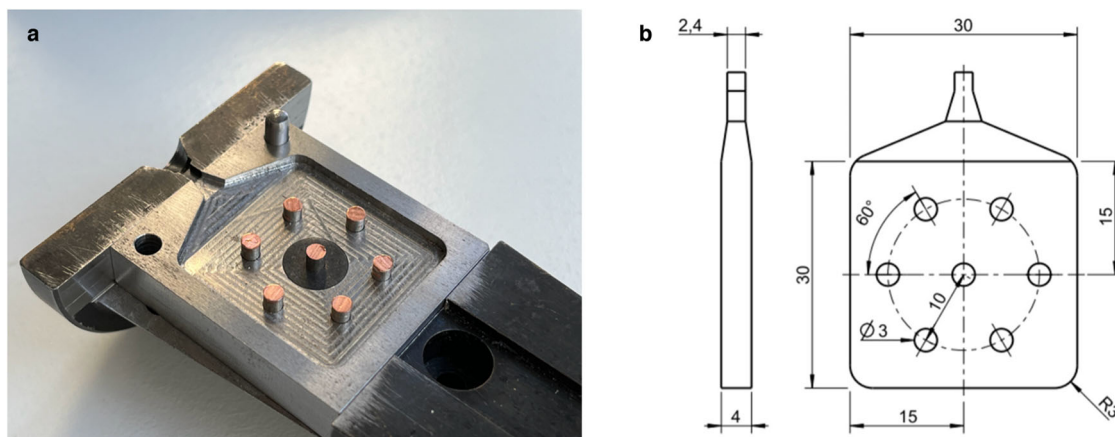
Fig. 11 Injection mold details. a Mold half of the modular injection mold with integrated inserts. **b** Technical drawing of the specimen geometry without inserts.

Table 2 Injection molding parameters.

		PP CF30	PA CF30
Cylinder temperature	in °C	260	290
Mold temperature	in °C	60	100
Injection time	in s	2	2
Injection pressure	in bar	300	600
Packing time	in s	20	20

Advanced Materials, Basel, Switzerland). After curing the resin for 12 h, the examination area was polished with a manual wet grinder (TG 250, Jean Wirtz, Dusseldorf, Germany) using progressively finer abrasive paper up to P4000 grit. The specimen was ground until the target plane was reached on half of the specimen at 2 mm. After cleaning in an ultrasonic bath to remove possible contamination from conductive carbon, copper or insulating polymer matrix particles, the specimens appear as in Fig. 1c.

Reflected light microscopic imaging. To create the high-resolution light microscopic images, a digital microscope (VHX 7000, KEYENCE, Osaka, Japan) was used. An optical magnification of 100x was set with a ring light illumination and the E100 objective. In order to be able to capture the large surface area of 30 mm × 30 mm at this magnification, the automatic stitching function of the microscope was applied. In addition, the depth of field option was set to achieve optimal image sharpness. These settings resulted in images with a resolution of about 32,000 × 39,000 px and a file size of over 350 MB. An exemplary image section of the area around the center insert is shown in Fig. 1d.

Image preparation. The basis is a microscopy image. If the image is in color, it should be converted to grayscale (to reduce data size). The next step is to mask areas that are not to be analyzed, if there are any (such as inserts or casting resin, as in our example). This can be done with simple Matlab edge detection functions or manually (as in our example). If the image contains only fibers in a polymer matrix, nothing needs to be done. For better comparability of the two specimen, the two microscopic images were aligned, i.e. rotated by a few degrees.

Data availability
The data that support the findings of this study are available from the corresponding author upon reasonable request.

Code availability
All of the code from this current study is available at https://doi.org/10.5281/zenodo.8309950, including all of the examples described in this article with the necessary parameters for a recalculation with the option to use a colorblind friendly color map. The code was written in Matlab R2022b and uses the Parallel Computing Toolbox.

References
1. Mrazova, M. Advanced composite materials of the future in aerospace industry. *INCAS Bull.* **5**, 139–150 (2013).
2. Zhao, Q. et al. Review on the electrical resistance/conductivity of carbon fiber reinforced polymer. *Appl. Sci.* https://doi.org/10.3390/app9112390 (2019).
3. Unterweger, C., Brüggemann, O. & Fürst, C. Synthetic fibers and thermoplastic short-fiber-reinforced polymers: Properties and characterization. *Polym. Compos.* **35**, 227–236 (2014).
4. Eckel, E. et al. Determination of local electrical properties using a potential field measurement for electrically conductive carbon fiber reinforced plastics with metal contact pins joined via injection molding. *Polymers* **14**, 2805 (2022).
5. Schneidmadel, S., Koch, M. & Bruchmüller, M. Effects of fiber orientation on the electrical conductivity of filled plastic melt. *AIP Conf. Proc.* **1779**, 030007 (2016).
6. Heim, H.-P., Mieth, F., Schlink, A., Wiegel, K. & Brabetz, L. Joining of contact pins and conductive compounds via injection molding—influence of the flow situation on the electrical contact resistance. *Int. Polym. Process.* **35**, 184–192 (2020).
7. Kirkpatrick, S. Percolation and conduction. *Rev. Mod. Phy.* **45**, 574 (1973).
8. Lux, F. Models proposed to explain the electrical conductivity of mixtures made of conductive and insulating materials. *J. Mater. Sci.* **28**, 285–301 (1993).
9. Bernasconi, A., Carboni, M. & Ribani, R. On the combined use of digital image correlation and micro computed tomography to measure fibre orientation in short fibre reinforced polymers. *Compos. Sci. Technol.* **195**, 108182 (2020).
10. Wilhelmsson, D. & As p, L. E. A high resolution method for characterisation of fibre misalignment angles in composites. *Compos. Sci. Technol.* **165**, 214–221 (2018).
11. Land, P., Krumpholz, T. & Heim, H.-P. Influencing the fibre orientation of polypropylene and polyamide in the injection moulding process by a rotating mould core. *J. Plastics Technol.* https://doi.org/10.3139/O999.03032022 (2022).
12. Vélez-García, G. M., Wapperom, P., Kunc, V., Baird, D. G. & Zink-Sharp, A. Sample preparation and image acquisition using optical-reflective microscopy in the measurement of fiber orientation in thermoplastic composites. *J. Microsc.* **248**, 23–33 (2012).
13. Davidson, N. C., Clarke, A. R. & Archenhold, G. Large-area, high-resolution image analysis of composite materials. *J. Microsc.* **185**, 233–242 (1997).
14. Sharp, N., Goodsell, J. & Favaloro, A. Measuring fiber orientation of elliptical fibers from optical m`-+icroscopy. *J. Compos. Sci.* **3**, 23 (2019).
15. Yurgartis, S. W. Measurement of small angle fiber misalignments in continuous fiber composites. *Compos. Sci. Technol.* **30**, 279–293 (1987).
16. Kastner, J. et al. Advanced X-Ray tomographic methods for quantitative characterisation of carbon fibre reinforced polymers. In *4th International Symposium on NDT in Aerospace* (AeroNDT, 2012).

17. Yang, X., Ju, B., Kersemans, M. *Ultrasonic Reconstruction of the Fiber Architecture of Composite Laminates.* https://www.ndt.net/article/ndtp2021/papers/Ultrasonic_Reconstruction_of_the_Fiber_Architecture_of_Composite_Laminates.pdf (2021).

18. Fereshteh-Saniee, N. et al. Quality analysis of weld-line defects in carbon fibre reinforced sheet moulding compounds by automated eddy current scanning. *J. Manuf. Mater.* **6**, 151 (2022).

19. Hughes, R. R., Drinkwater, B. W. & Smith, R. A. Characterisation of carbon fibre-reinforced polymer composites through radon-transform analysis of complex eddy-current data. *Compos. B. Eng.* **148**, 252–259 (2018).

20. Jafari-Khouzani, K. & Soltanian-Zadeh, H. Radon transform orientation estimation for rotation invariant texture analysis. *IEEE Trans. Pattern Anal.* **27**, 1004–1008 (2005).

21. Krause, M., Marcel Hausherr, J. & Krenkel, W. Computing the fibre orientation from radon data using local radon transform. *Inverse Probl. Imaging* **5**, 879–891 (2011).

22. Schaub, N. J., Kirkpatrick, S. J. & Gilbert, R. J. Automated methods to determine electrospun fiber alignment and diameter using the radon transform. *BioNanoScience* **3**, 329–342 (2013).

23. Yang, X., Ju, B., Kersemans, M. Assessment of the 3D ply-by-ply fiber structure in impacted CFRP by means of planar Ultrasound Computed Tomography (pU-CT). *Compos. Struct.* **279**, 114745 (2022).

24. Li, X. et al. Prediction of residual strains due to in-plane fibre waviness in defective carbon-fibre reinforced polymers using ultrasound data. *J. Nondestruct. Eval.* **42**, 2 (2022).

25. Kratmann, K. et al. A novel image analysis procedure for measuring fibre misalignment in unidirectional fibre composites. *Compos. Sci. Technol.* **69**, 228–238 (2009).

26. Creighton, C., Sutcliffe, M. & Clyne, T. A multiple field image analysis procedure for characterisation of fibre alignment in composites. *Compos. A: Appl. Sci. Manuf.* **32**, 221–229 (2001).

27. Sutcliffe, M., Lemanski, S. L. & Scott, A. E. Measurement of fibre waviness in industrial composite components. *Compos. Sci. Technol.* **72**, 2016–2023 (2012).

28. Żurawik, R., Volke, J., Zarges, J.-C. & Heim, H.-P. Comparison of real and simulated fiber orientations in injection molded short glass fiber reinforced polyamide by X-ray microtomography. *Polymers* **14**, 29 (2021).

Author contributions
K.W., A.S. and E.E. designed the experiments. K.W., A.S. and L.B. developed the methodology. K.W. developed the software code. K.W. and A.S. validated the method. A.S. prepared the samples and performed the structural analysis. M.A., L.B. and H.-P.H. provided the resources. K.W., A.S. and E.E. curated the data. K.W. and A.S. wrote the original draft. E.E., M.A., L.B., M.H. and H.-P.H. reviewed and edited the paper. K.W. and A.S. created the visualizations. M.A., L.B., M.H. and H.-P.H. supervised and administrated the project. K.W., A.S., M.A., L.B. and H.-P.H. obtained the funding. All authors have read and agreed to the published version of the manuscript. All authors contributed to data analysis and scientific discussion. All authors reviewed, edited, and approved the manuscript.

Competing interests
The authors declare no competing interests.

Additional information
Supplementary information The online version contains supplementary material available at https://doi.org/10.1038/s43246-023-00403-1.

Correspondence and requests for materials should be addressed to Klara Wiegel or André Schlink.

Peer review information *Communications Materials* thanks the anonymous reviewers for their contribution to the peer review of this work. Primary Handling Editor: John Plummer. A peer review file is available.

Reprints and permission information is available at http://www.nature.com/reprints

Publisher's note Springer Nature remains neutral with regard to jurisdictional claims in published maps and institutional affiliations.